Electronic Supplementary Material (ESI) for Chemical Science.
This journal is © The Royal Society of Chemistry 2024

Electronic Supplementary Information for

# Atomically dispersed dinuclear iridium active sites for efficient and stable electrocatalytic chlorine evolution reaction

*Zhipeng Yu,[‡a, b] Guangjie Xia,[‡c,d] Vlad Martin Diaconescu,[e] Laura Simonelli,[e] Alec P. LaGrow,[b,f] Zhixin Tai,[b] Xinyi Xiang,[a] Dehua Xiong,[g] and Lifeng Liu[*a]*

[a] *Songshan Lake Materials Laboratory, Dongguan 523808, P.R. China*

[b] *International Iberian Nanotechnology Laboratory (INL), Avenida Mestre Jose Veiga, 4715-330 Braga, Portugal*

[c] *School of Physical Sciences, Great Bay University, Dongguan 523808, P.R. China*

[d] *Great Bay Institute for Advanced Study, Dongguan, 523000, P.R. China*

[e] *ALBA Synchrotron, Carrer Llum 2-26, Cerdanyola del Valles, Barcelona 08290, Spain*

[f] *Scientific Imaging Section, Okinawa Institute of Science and Technology Graduate University, Kunigami-gun, Okinawa 904-0412, Japan*

[g] *State Key Laboratory of Silicate Materials for Architectures, Wuhan University of Technology, Wuhan 430070, P. R. China*

‡ These authors contribute equally to this work.

* Corresponding author email. liu.lifeng@sslab.org.cn (L.L.)

## Experimental procedures

## Reagents

$Zn(NO_3)_2{\cdot}6H_2O$, 2-methylimidazole (2-MeIM), methanol, isopropanol, $HClO_4$, NaCl, iridium(III) acetylacetonate ($Ir(acac)_3$) and Nafion® perfluorinated resin solution (5 wt %) were all purchased from Sigma-Aldrich. (1,5-Cyclooctadiene)(methoxy)iridium(I) dimer ($[Ir(OCH_3)(C_8H_{12})]_2$) was bought from Tokyo Chemical Industry Co., Ltd. Commercial dimensionally stable anodes (DSA, $IrO_2$-$RuO_2$-$TiO_2$) were purchased from Baoji Highstar Titanium Metal Co.,Ltd., China. All reagents and materials were used as received without further purification or treatment.

## Materials Synthesis

**Synthesis of ZIF-8, ZIF-8@$Ir_1$ and ZIF-8@$Ir_2$**. The ZIF-8 materials were synthesized via a method reported previously with some modification.[1] Typically, 594 mg of $Zn(NO_3)_2{\cdot}6H_2O$ were dissolved in 20 mL methanol under vigorous magnetic stirring to form a homogeneous solution A. In the meantime, 659 mg of 2-MeIM were dissolved in 15 mL methanol forming a solution B. Then, solutions A and B were mixed under vigorous stirring for 1 h. Subsequently, the mixed solution was transferred into a Teflon-lined stainless steel autoclave reactor, which was heated up to 60 °C and maintained at this temperature for 4 h. The obtained product was centrifuged, washed five times with methanol, and then dried under vacuum at 60 °C for further use. The ZIF-8@$Ir_1$ catalysts were synthesized using the same procedure as described above with the addition of $Ir(acac)_3$ in solution A. It is worth noting that $[Ir(OCH_3)(C_8H_{12})]_2$ is sensitive to oxygen and light, and therefore the synthesis of ZIF-8@$Ir_2$ should be carried out under $N_2$ atmosphere in the dark through a similar procedure but using $[Ir(OCH_3)(C_8H_{12})]_2$ as Ir precursors. Specifically, $Zn(NO_3)_2{\cdot}6H_2O$ and $[Ir(OCH_3)(C_8H_{12})]_2$ were dissolved in methanol under vigorous magnetic stirring for 24 h to form a homogeneous solution A under $N_2$ atmosphere. Meanwhile, 2-MeIM were dissolved in methanol to obtain a solution B. Afterward, solutions A and B were mixed under constant stirring for 1 h and were then transferred into a Teflon-lined stainless steel autoclave reactor for sovlothermal reaction.

**Synthesis of NC, $Ir_1$-NC and $Ir_2$-ONC**. The obtained ZIF-8 powders were loaded in a ceramic boat that was placed in a tube furnace filled with high-purity $N_2$ (99.999%). The furnace was heated to 900 °C at a rate of 5 °C $min^{-1}$, held at this temperature for 1 h, and then naturally cooled down to room temperature under a constant $N_2$ flow in the whole process. The $Ir_1$-NC and $Ir_2$-ONC catalysts were obtained through a similar procedure as that used to synthesize NC, except that the starting material was replaced by ZIF-8@$Ir_1$ and ZIF-8@$Ir_2$, respectivley.

## Materials characterization

Powder X-ray diffraction (XRD) examinations were conducted on an X'Pert PRO diffractometer (PANalytical) working at 45 kV and 40 mA with Cu $K_\alpha$ radiation (λ = 1.541874 Å) and a PIXcel detector. Data were collected with the Bragg-Brentano configuration in the 2θ range of 20 – 90° at a scan speed of 0.01° $s^{-1}$. X-ray photoelectron spectroscopy (XPS) characterization was performed on an ESCALAB 250Xi instrument with an Al $K_\alpha$ X-ray source (1486.6 eV). Nitrogen adsorption/desorption

porosimetry measurements were conducted using a Quantachrome Autosorb IQ2 system at 77 K. The surface area of samples was derived from the Brunauer-Emmett-Teller (BET) method. The morphology was characterized by scanning electron microscopy (SEM, FEI Quanta 650 FEG microscope equipped with an INCA 350 spectrometer). *In-situ* Raman spectroscopy examination was done on a confocal Raman spectrometer (Horiba LabRam HR Evolution). Scanning transmission electron microscopy (STEM) investigations were carried out on a probe-corrected transmission electron microscope operating at 200 kV (FEI Themis 60 – 300). The actual metal contents of Ir were detected by the inductively coupled plasma – optical emission spectroscopy (ICP-OES, ICPE-9000 spectrometer, Shimadzu). The X-ray absorption spectroscopy (XAS) was conducted at the BL22-CLAESS beamline, ALBA Synchrotron (Barcelona, Spain). Data was acquired with a Si311 DCM in transmission mode at room temperature. Samples were prepared as pellets in cellulose. The Athena software package was used for spectra processing. The energy was calibrated to the first inflection point of $Ir^0$ taken as 11215 eV. EXAFS were extracted with the AUTOBK algorithm in the 3-12 $A^{-1}$ *k*-range having an Rbkg of 1.1. Then the FT parameters can be refereced in the picture where it is shown.

## DFT calculations

The spin-polarized density functional theory (DFT) calculations were applied within the framework of periodic boundary conditions using the VASP code.[2] The ion–core electron interaction was described by the projected augmented wave method,[3] and the exchange and correlation interactions by the PBE functional.[4] Dispersion interactions were introduced by applying D3 corrections.[5] As the model system is considerably large with a periodic box of 17.22 Å × 17.04 Å × 18.40 Å, the Gamma point k-point sampling was conducted, and the energy cutoff was set to 400 eV. The convergence criterion for total energies was $10^{-7}$ eV with the Gaussian smearing scheme of 0.05 eV, while the forces acting on atoms were smaller than 0.02 eV/Å for geometry optimization. For simulations in the presence of explicit solvent water, the constrained ab initio molecular dynamic (AIMD) simulations were carried out using Nosé-Hoover thermostats[6] at room temperature (300 K) under the canonical (NVT) ensemble. The free energy barrier of $Cl^-$ substitution and adsorption step was obtained by the thermodynamic integral (TI) method[7] where 12 points were selected along the constrained Ir–Cl distances. For each constrained AIMD, to assist the fast equilibrium the initial configuration was obtained by a slow-growth simulation of 1.0 × $10^{-3}$ Å $fs^{-1}$. The deuterium mass was adopted to all the H atoms for the longer timestep of 1 fs. At each point, the simulation proceeded for 3.5 ps, during which the first 0.5 ps was dedicated to thermal equilibrium, while the subsequent 3 ps was used to obtain the free energy gradients.

The CER proceeds through the two-electron pathways with the following reaction steps:

$2Cl^- + * \rightarrow Cl^* + e^- + Cl^-$ (S1)

$Cl^* + Cl^- \rightarrow * + Cl_2 \uparrow + e^-$ (S2)

where the asterisk (*) represents the active site on the model catalysts of $Ir_1N_6$ and $Ir_2O_2N_8$, and "Cl*" denotes the corresponding chemisorbed species residing on the model catalyst surfaces.

## Electrode preparation and electrocatalytic tests.

The catalyst ink was prepared by ultrasonically dispersing 5 mg of catalysts into 0.5 mL of isopropanol containing 50 µL of Nafion® solution (5 wt%, Merck). To prepare an electrode for catalytic tests, 20 µL of catalyst ink was loaded on a fine-polished glassy carbon (GC) electrode with an exposed area of 0.50 $cm^2$, leading to a loading mass of ca. 0.36 mg $cm^{-2}$. The electrode was then dried at room temperature (ca. 25 °C) naturally in air.

All electrocatalytic tests of half reactions were carried out in a three-electrode configuration at room temperature (23 °C) using a Biologic VMP-3 potentiostat/galvanostat. The catalyst-loaded GC, a graphite rod and a saturated calomel electrode (SCE) were used as working, counter, and reference electrodes, respectively. The SCE reference electrode was calibrated prior to each measurement in an Ar/$H_2$-saturated 0.5 M $H_2SO_4$ solution using a clean Pt wire as the working electrode. The CER measurements were carried out in 0.1 M $HClO_4$ + 4 M NaCl. Unless otherwise stated, all potentials are reported versus normal hydrogen electrode (NHE) by converting the measured potentials according to the following equation:

$$E_{NHE} = E_{SCE} + 0.241 \quad \text{(S3)}$$

The apparent CER activity was characterized using cyclic voltammetry (CV) at a scan rate of 5 mV $s^{-1}$, and an *iR*-correction (85%) was made to compensate for the voltage drop between the reference and working electrodes, which was measured by a single-point high-frequency impedance test. The electrochemical impedance spectroscopy (EIS) measurements were conducted at 1.443 V *vs.* NHE in the frequency range of $10^5$ – 0.01 Hz with a 10 mV sinusoidal perturbation. The electrocatalytically active surface areas (ECSAs) were calculated from the electrochemical double-layer capacitance of the catalyst's surface. The double-layer capacitance ($C_{dl}$) of catalysts was estimated by performing CV in the non-Faradaic potential range of 0.34 to 0.54 V *vs.* NHE at different scan rates ($v$) of 10, 20, 30, 40, 50, 60, 70, 80, 90 and 100 mV $s^{-1}$, followed by extracting the slope from the resulting $|j_a\text{-}j_c|/2$ *vs. v* plots ($j_a$ and $j_c$ represent the anodic and cathodic current at 0.44 V *vs.* NHE).[8] The ECSA was estimated upon dividing $C_{dl}$ by the capacitance of a model catalyst over a unit surface area (usually 0.035 mF $cm^{-2}$ for noble metals)[8, 9], as follows:

$$\text{ECSA} = C_{dl} / 0.035 \text{ mF cm}^{-2} \quad \text{(S4)}$$

The CER stability of $Ir_2$-ONC catalysts was assessed at a constant current density of 10 mA $cm^{-2}$. The accelerated stress test (AST) of CER was performed in the potential range of 1.04 – 1.44 V *vs.* NHE at 100 mV $s^{-1}$ for continuous 40000 cycles. The turnover frequency (TOF) of the catalysts was calculated according to the following formula:[10]

$$\text{CER: } TOF = \frac{j}{2nF} \quad \text{(S5)}$$

where $j$ (A) is the current at a given overpotential, $F$ = 96500 C $mol^{-1}$ stands for the Faraday constant, and $n$ (mol) is mole number of Ir loaded on the GC electrode. All metal species in catalysts were assumed to be catalytically active, so the calculated values represent the lower limits of TOF.

The Faradaic efficiency of the CER was determined through iodometric titration, as illustrated in Figure S13a. Chronoamperometry (CA) was firstly conducted at 1.42, 1.44, and 1.46 V vs. NHE for a duration of 1200 s in a 0.1 M $HClO_4$ + 4.0 M NaCl electrolyte. The anolyte was then mixed excess NaI to minimize the equilibrium concentration of volatile $I_2$, which made the anolyte rapidly change its color to yellowish-brown (equation S6). Subsequently, the generated $I_2$ was titrated with a standard 0.01 M $Na_2S_2O_3$ solution (equation S7). When the solution color turned to pale brown, a starch indicator was added, making the solution change its color to dark blue. The titration process then continued by adding more $Na_2S_2O_3$ until the solution became clear and colorless. Equations S8 to S10 are used to compute the experimental and theoretical yields of $Cl_2$, as well as the selectivity of the CER.

$Cl_2 + 2NaI \rightarrow I_2 + 2NaCl$ (S6)

$I_2 + 2Na_2S_2O_3 \rightarrow Na_2S_4O_6 + 2NaI$ (S7)

$$\text{Experimental yield (mol)} = \frac{0.01\ \text{M} \times \text{Volume of } Na_2S_2O_3\ \text{(L)}}{2} \quad \text{(S8)}$$

$$\text{Theoretical yield (mol)} = \oint \frac{i}{2F} dt \quad \text{(S9)}$$

$$\text{The selectivity of } Cl_2 = \frac{\text{Experimental yield}}{\text{Theoretical yield}} \times 100\ \% \quad \text{(S10)}$$

**Supplementary figures**

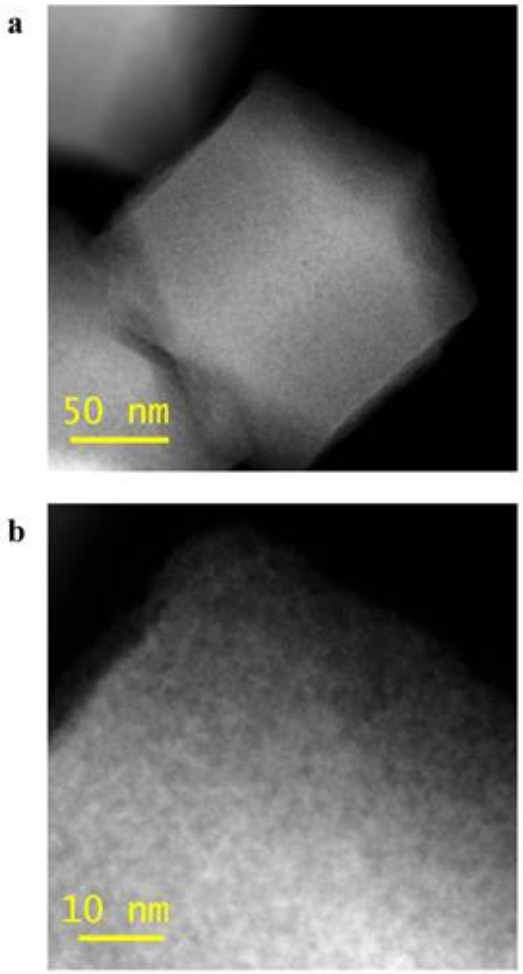


**Figure S1.** a, b) HAADF-STEM images showing the morphology of NC.

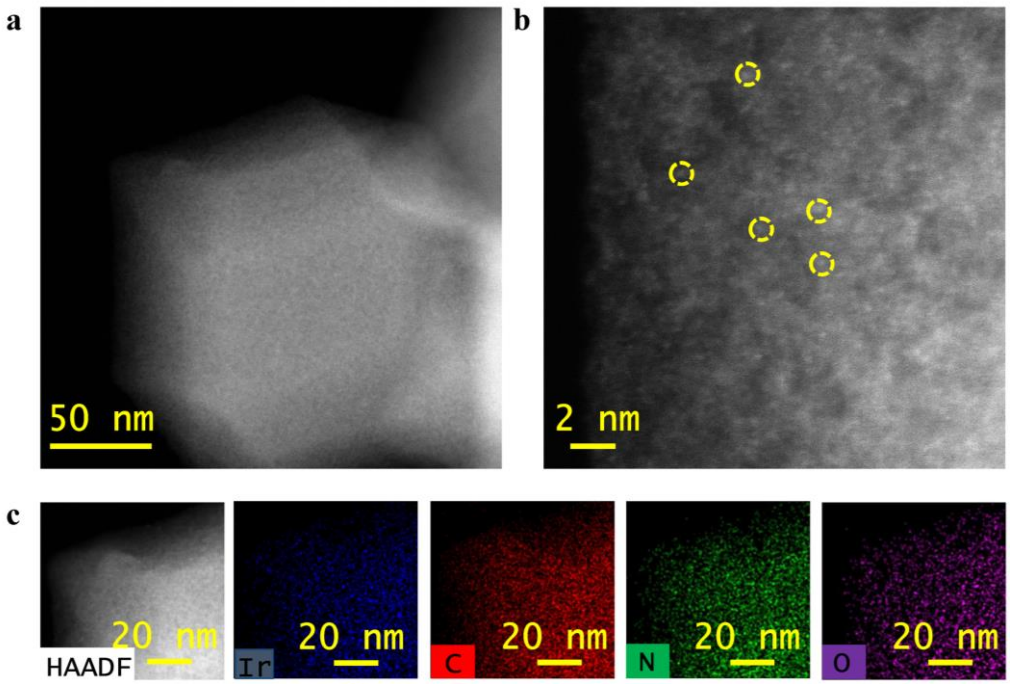


**Figure S2.** Morphology and microstructure characterization of $Ir_1$-NC catalysts. a, b) HAADF-STEM images at different magnifications. c) HAADF-STEM image and the corresponding elemental maps of Ir, C, N and O.

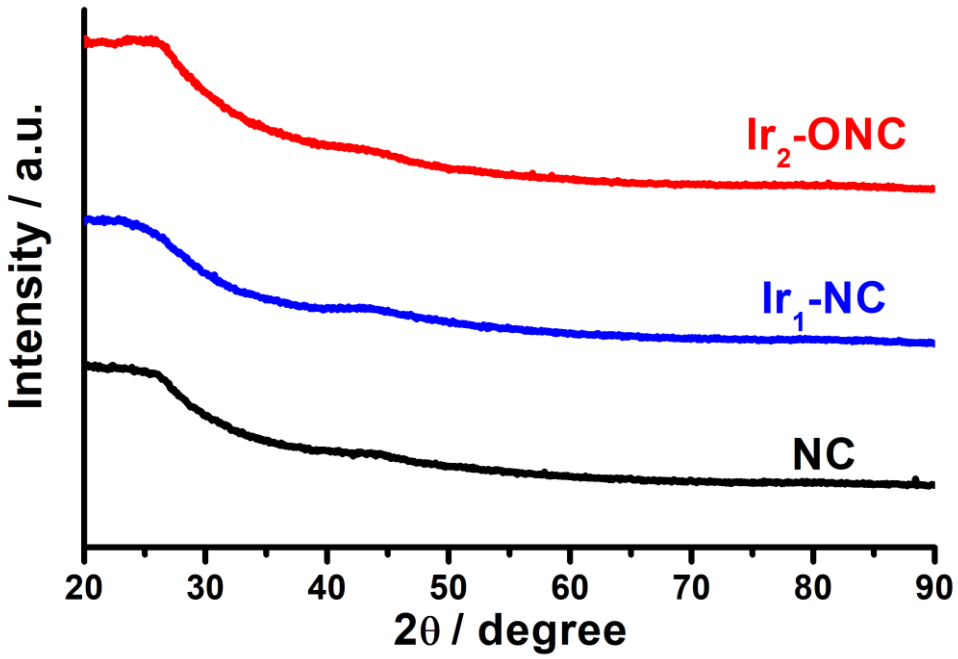


**Figure S3.** XRD patterns of NC, $Ir_1$-NC and $Ir_2$-ONC.

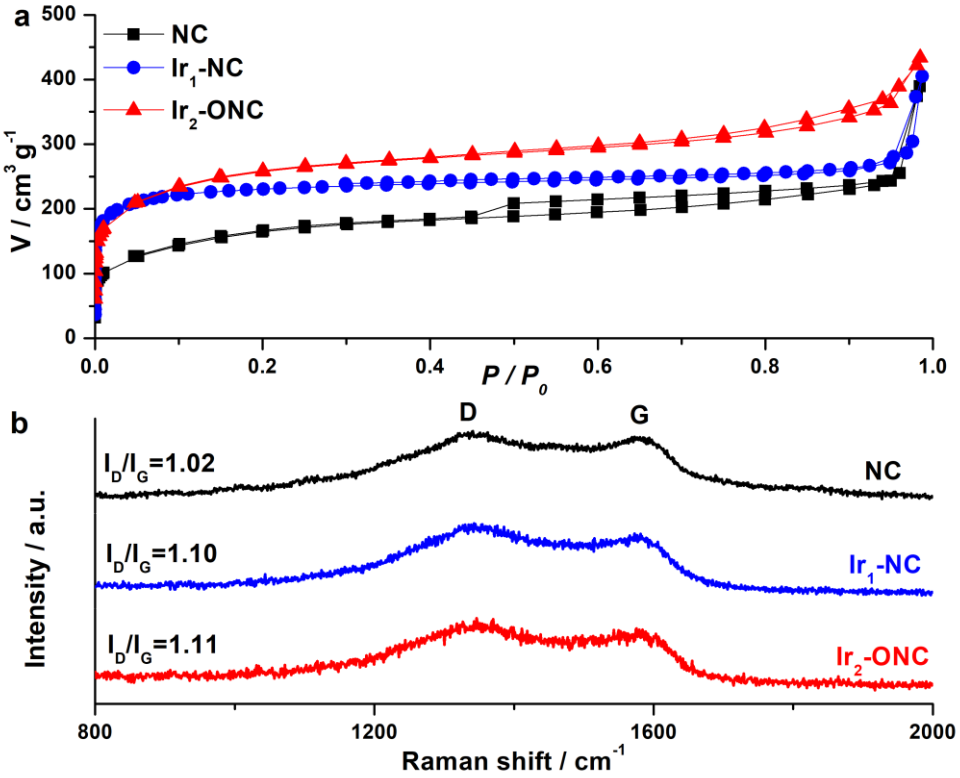


**Figure S4.** a) $N_2$ adsorption and desorption isotherms and b) Raman spectra of NC, $Ir_1$-NC and $Ir_2$-ONC.

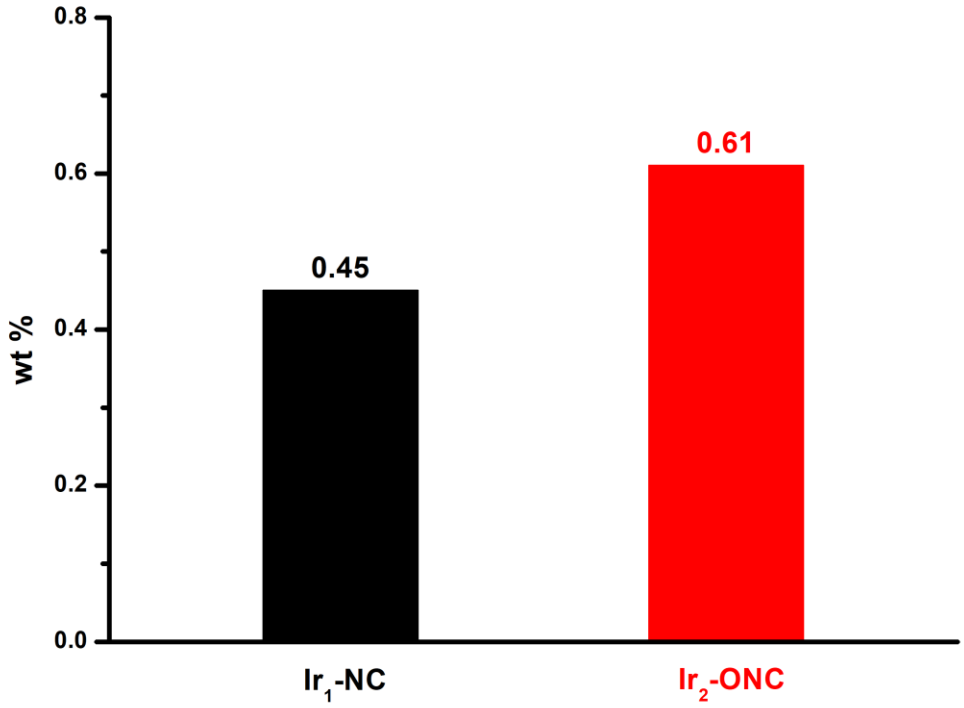


**Figure S5.** The actual metal contents in $Ir_1$-NC and $Ir_2$-ONC.

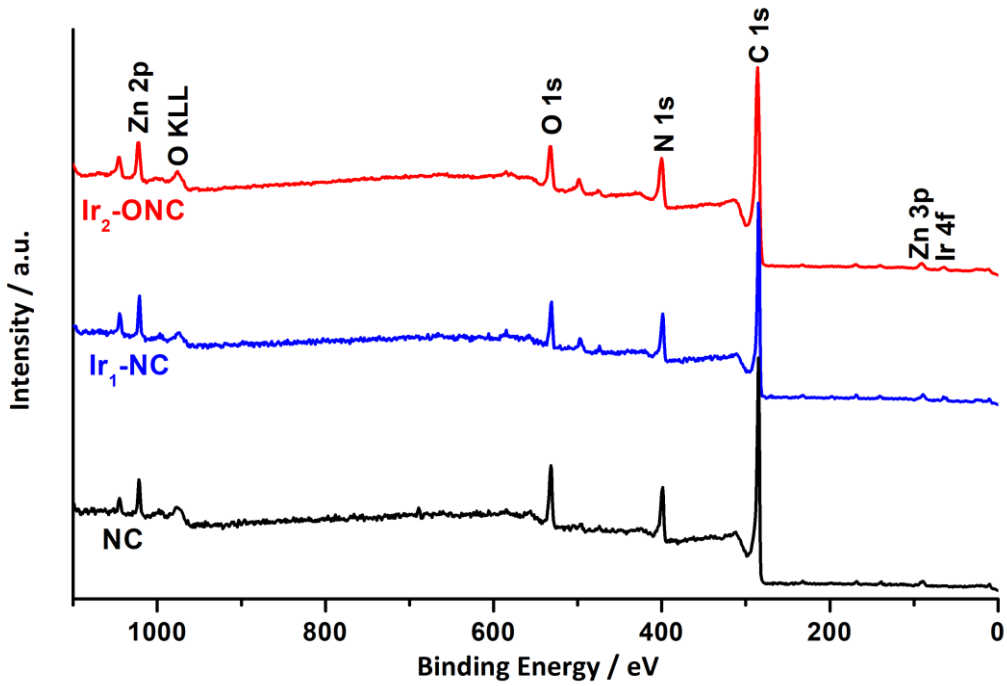


**Figure S6.** XPS survey spectra of NC, $Ir_1$-NC and $Ir_2$-ONC.

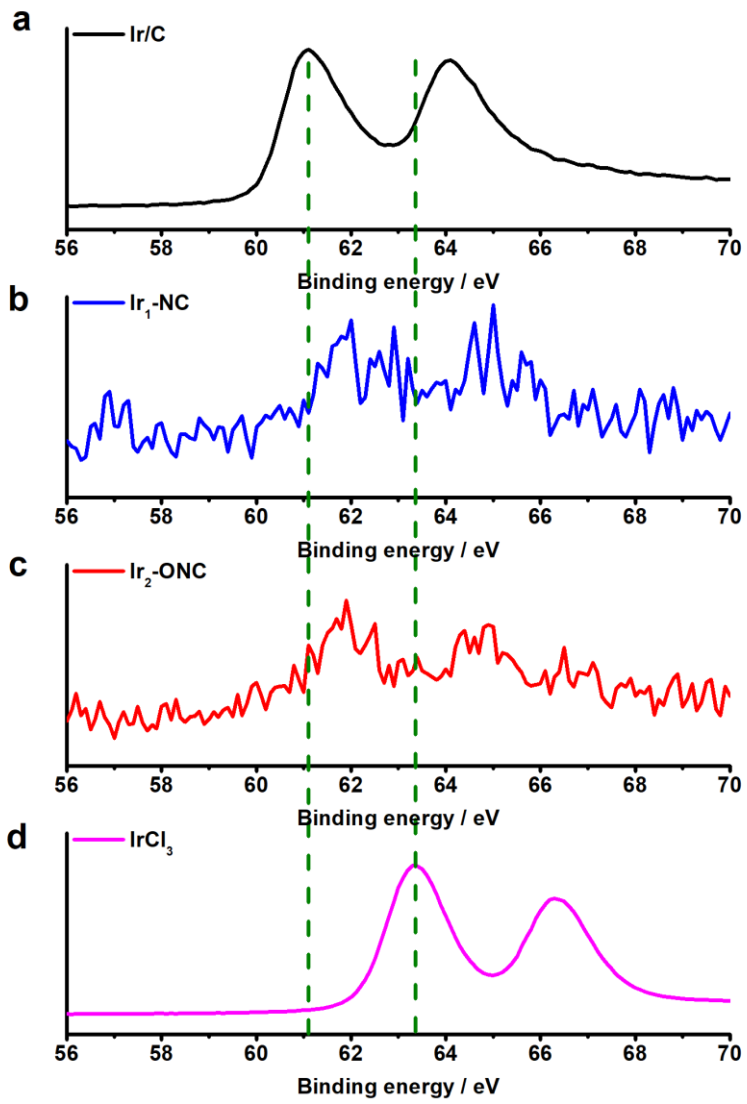


**Figure S7.** High-resolution Ir4f XPS spectra of a) Ir/C, b) $Ir_1$-NC, c) $Ir_2$-ONC and d) $IrCl_3$.

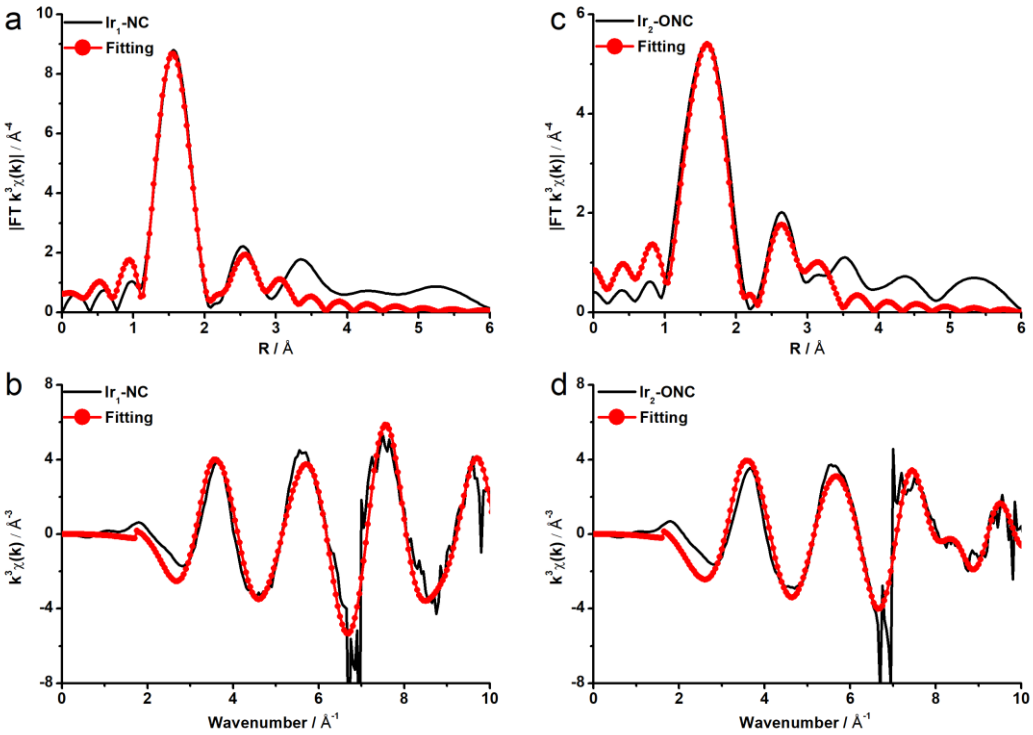


**Figure S8**. Ir $L_3$-edge EXAFS fitting curves of $Ir_1$-NC and $Ir_2$-ONC in a, c) *R* space and b, d) *k* space.

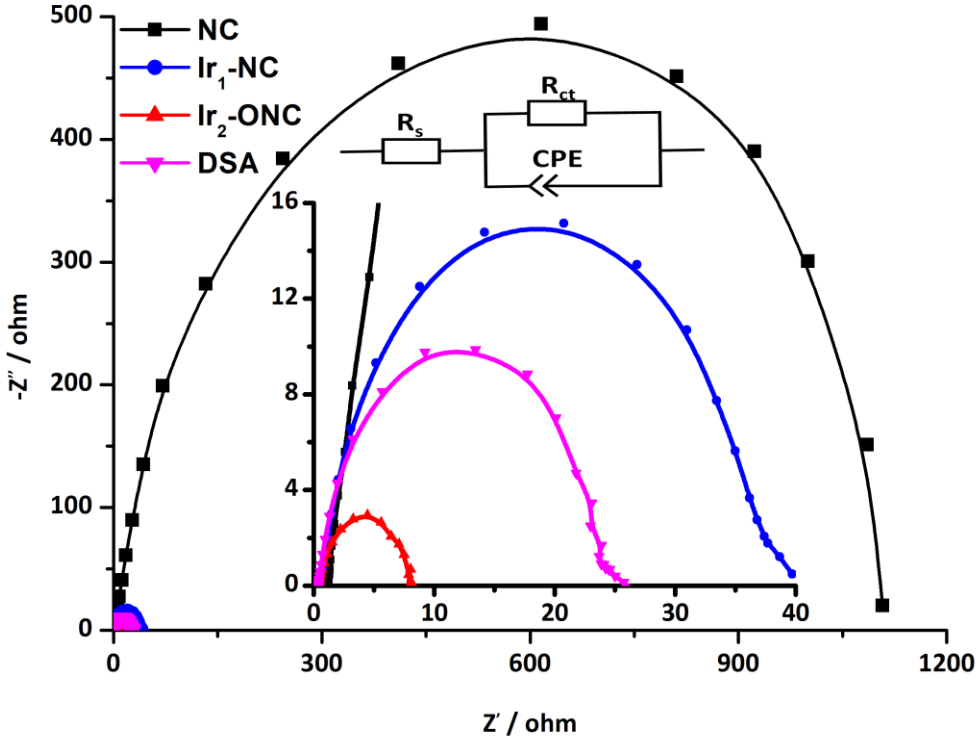


**Figure S9.** Nyquist plots of the $Ir_2$-ONC and reference catalysts measured at 1.443 V *vs.* NHE. Inset: the equivalent circuit model.

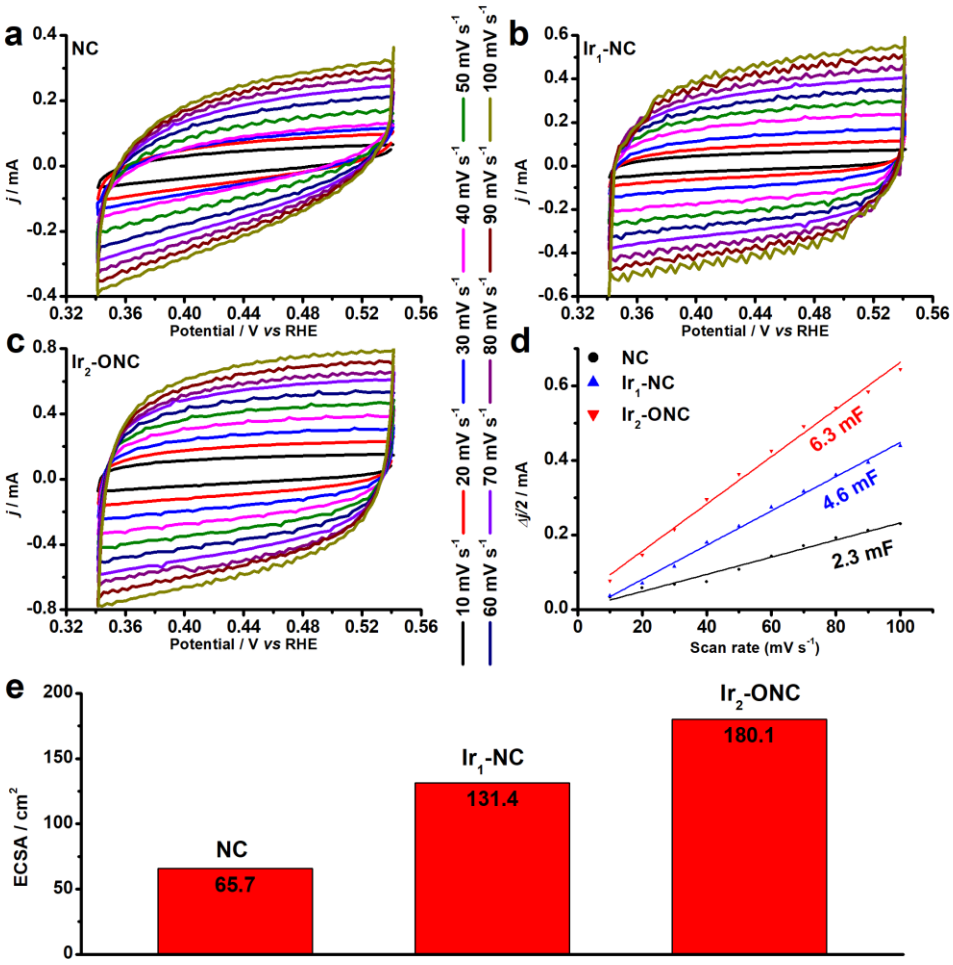


**Figure S10.** Electrochemical CV curves of a) NC, b) $Ir_1$-NC, c) $Ir_2$-ONC, recorded at different scan rates of 10, 20, 30, 40, 50, 60, 70, 80, 90, and 100 mV $s^{-1}$. d) Plots of the capacitive current as a function of the scan rate for all catalysts. e) ECSAs of all catalysts.

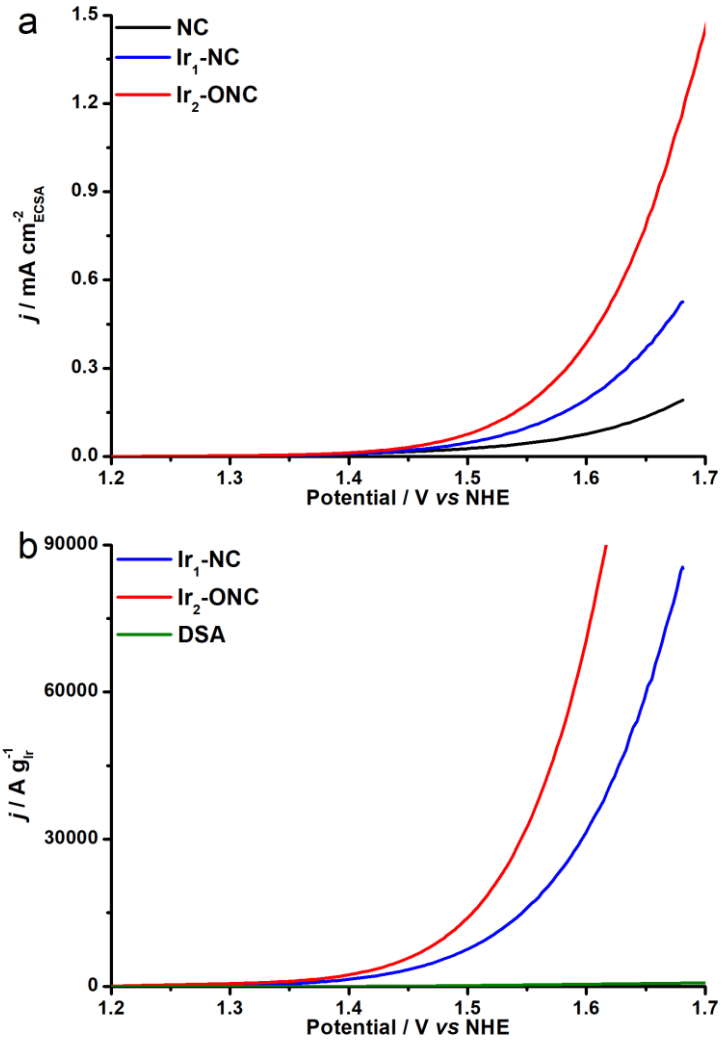


**Figure S11.** a) Specific activity and b) mass activity of $Ir_2$-ONC and reference catalysts.

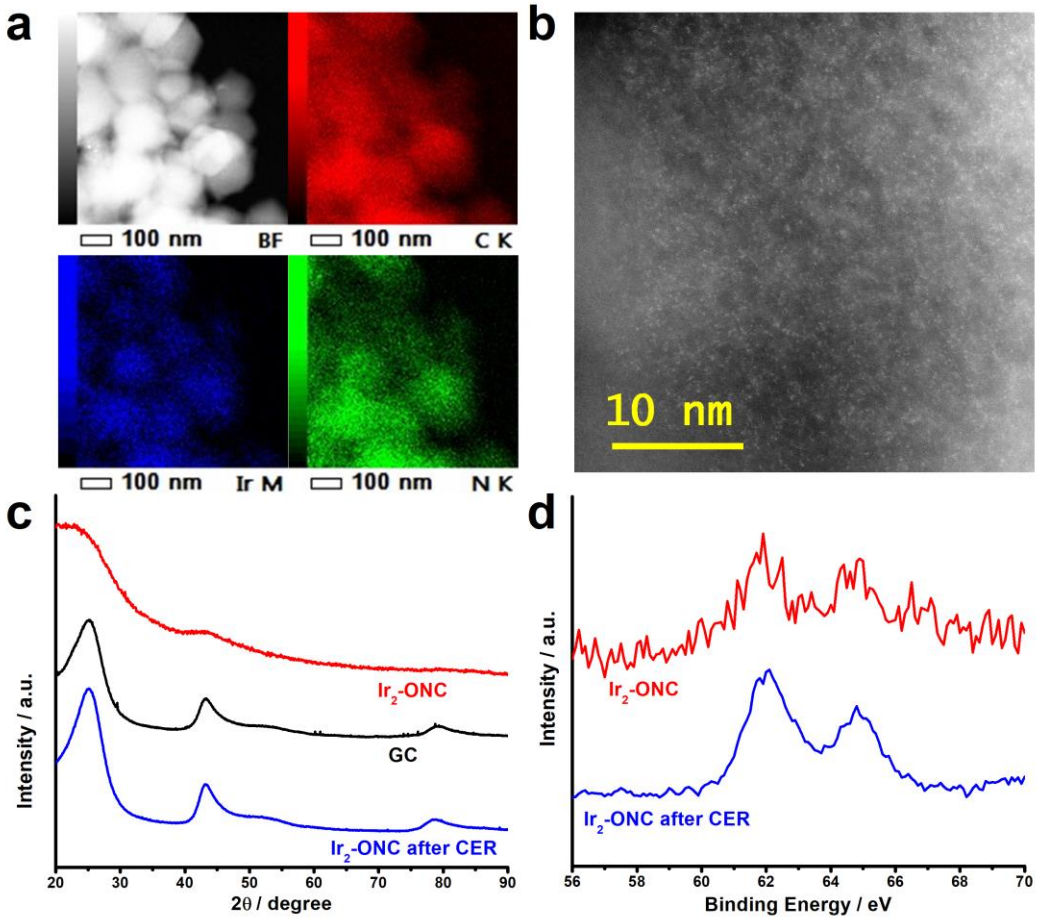


**Figure S12.** a) HAADF-STEM image and the corresponding elemental maps of Ir, C and N after the stability test (10 mA $cm^{-2}$, 20 h). b) High-resolution STEM image, c) XRD patterns and d) high-resolution Ir4f spectra of $Ir_2$-ONC after the stability test. The XRD pattern of $Ir_2$-ONC after the stability test was collected with a glassy carbon (GC) substrate as the support, and therefore the diffraction peaks from GC are clearly observed in the pattern. For comparison, the XRD pattern of a bare GC is presented.

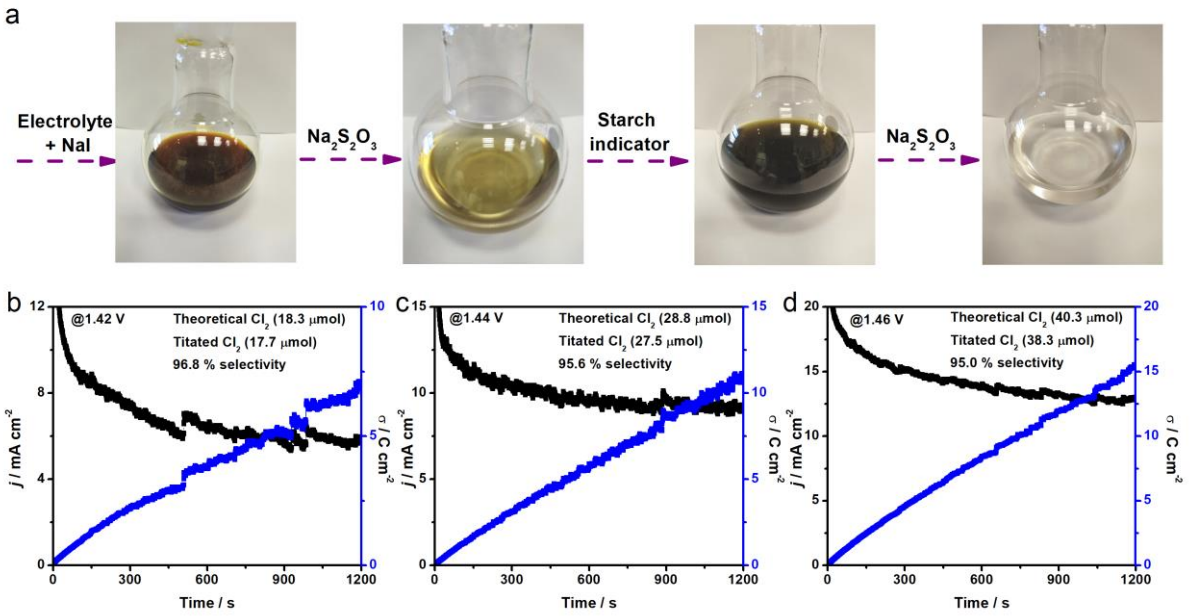


**Figure S13.** a) Illustration of the procedure of iodometric titration. Chronoamperograms for iodometric titration of $Cl_2$ produced on the $Ir_2$-ONC catalyst in 0.1 M $HClO_4$ + 4.0 M NaCl at b) 1.42 V, c) 1.44 V, and 1.46 V vs. NHE.

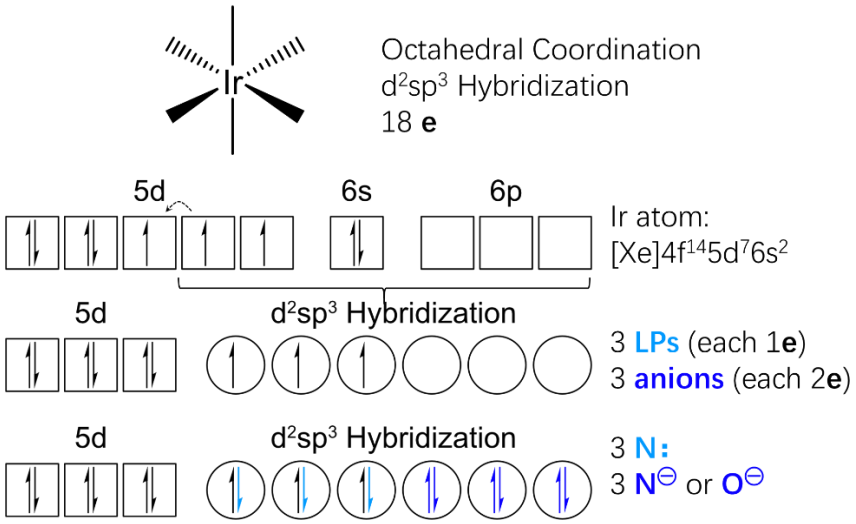


**Figure S14**. The hybridization of Ir (III) atom in the $Ir_1$-NC.

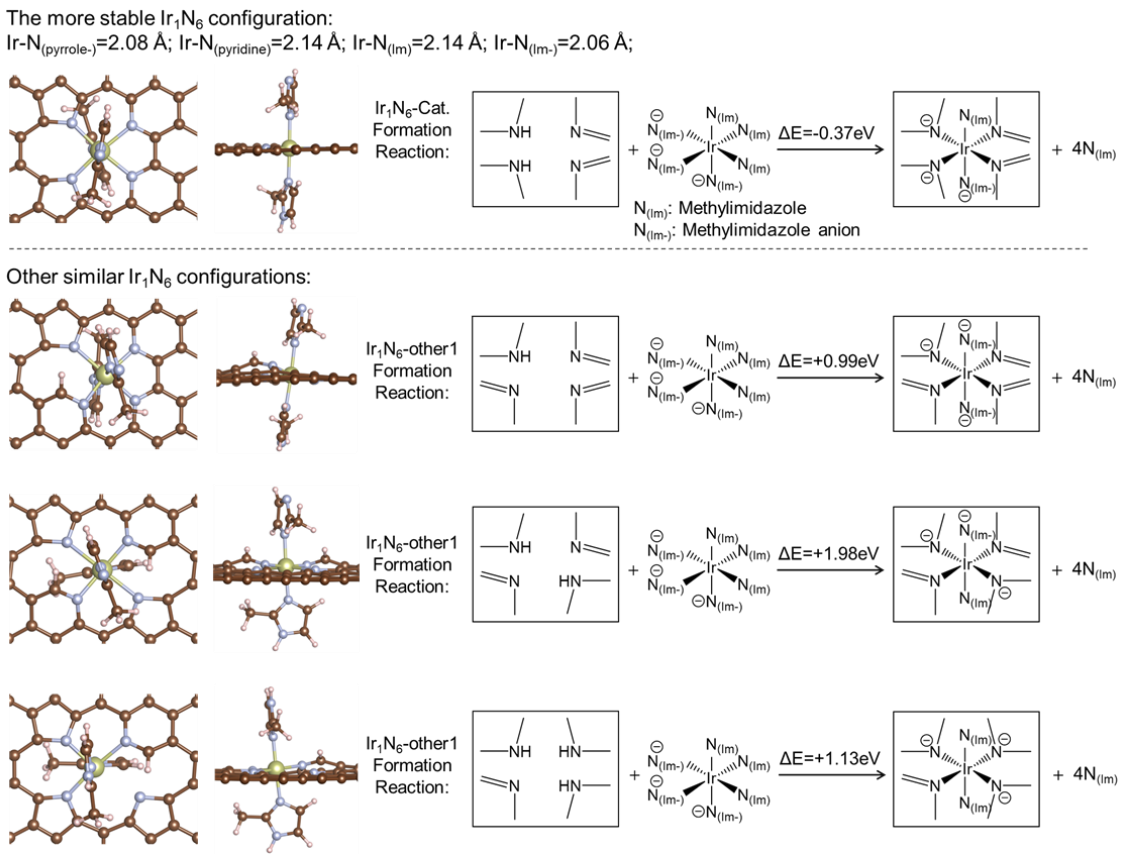


**Figure S15**. The formation energy calculation of the $Ir_1$-NC catalyst with different $Ir_1$-$N_6$ configurations. The left shows the top and side views of the 3D configurations of the $Ir_1$-NC catalyst. The light green, light blue, brown and white spheres represent Ir, N, C and H, respectively. The right shows the corresponding formation reactions from the experimentally used precursor.

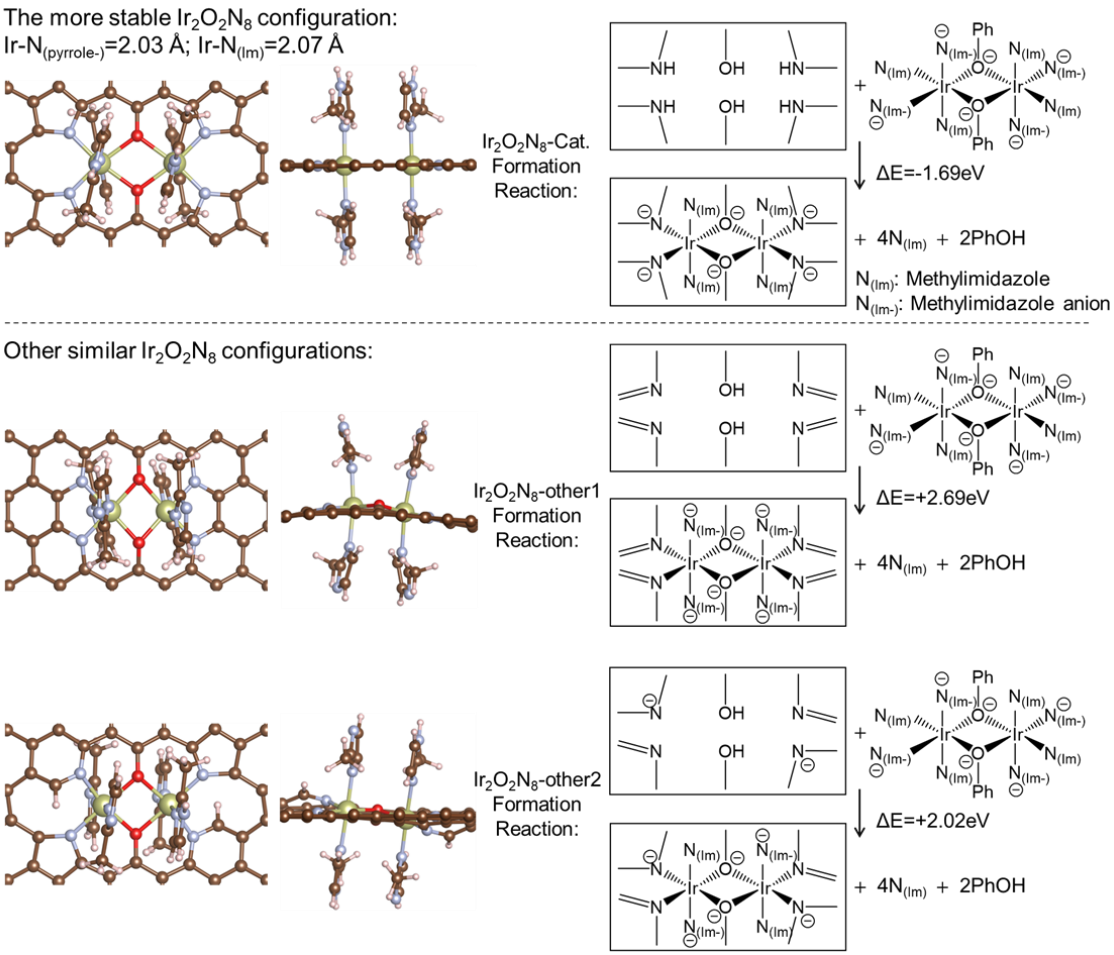


**Figure S16**. The formation energy calculation of the $Ir_2$-ONC catalyst with different $Ir_2O_2N_8$ configurations. The left shows the top and side views of the 3D configurations of the $Ir_2$-ONC catalyst. The light green, light blue, red, brown and white spheres represent Ir, N, O, C and H, respectively. The right shows the corresponding formation reactions from the experimentally used precursor.

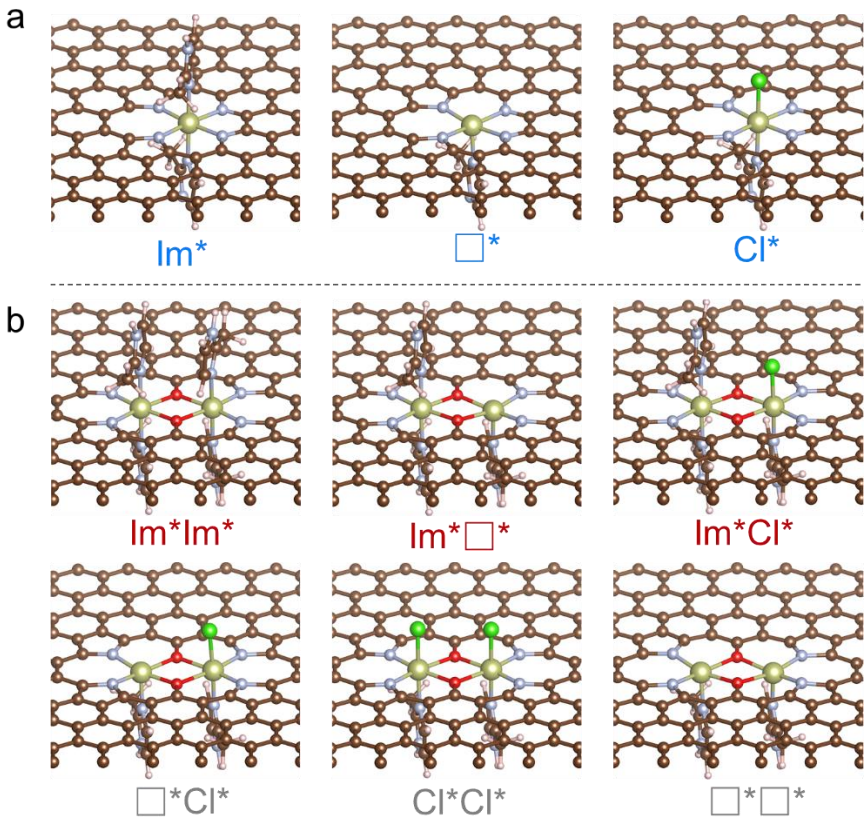


**Figure S17**. The 3D configurations of a) the $Ir_1$-NC catalyst and b) the $Ir_2$-ONC catalyst during the chlorine evolution reaction. The light green, light blue, red, brown, white and green spheres represent Ir, N, O, C, H and Cl, respectively.

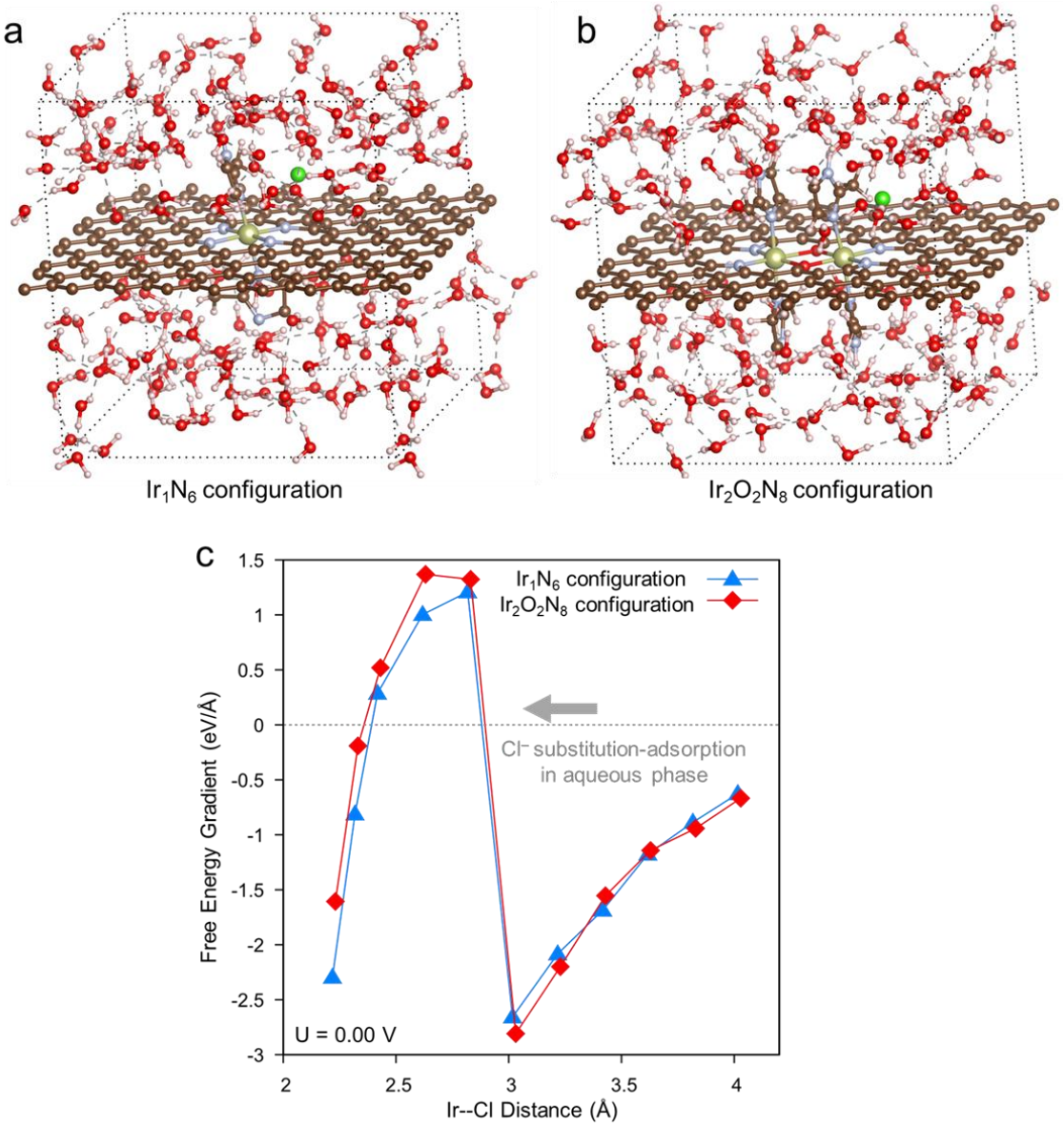


**Figure S18**. a) The $Ir_1N_6$ and b) $Ir_2O_2N_6$ models used for the AIMD simulations in aqueous solution. The light green, light blue, red, brown, white and green spheres represent Ir, N, O, C, H and Cl, respectively. c) Free energy gradient of the thermodynamic integral along the $Cl^-$ adsorption and substitution steps in the presence of explicit solvent water.

## Supplementary Tables:

**Table S1**. Fitting results of the N1s spectra of the pristine NC, $Ir_1$-NC and $Ir_2$-ONC catalysts.

| Sample | De-convoluted peaks | | | | |
|---|---|---|---|---|---|
| | **Pyridinic N** | **M–N** | **Pyrrolic N** | **Graphitic N** | **Oxyl-N** |
| **NC** | 40.6 | / | 11.0 | 25.2 | 23.2 |
| **$Ir_1$-NC** | 36.8 | 24.6 | 15.1 | 19.1 | 4.4 |
| **$Ir_2$-ONC** | 32.6 | 26.7 | 15.3 | 22.1 | 3.3 |

**Table S2**. Ligand structure parameters extracted from quantitative EXAFS curve-fitting.

| Samples | Path | CN | R / Å | $\sigma^2 \times 10^3$ / Å$^2$ | $\Delta E_0$ | R factor |
|---|---|---|---|---|---|---|
| $Ir_1$-NC | Ir–N | 0.73 | 1.90 | 13.59 | 8.92 | 0.012 |
| | Ir–N | 5.42 | 2.04 | 4.97 | | |
| | Ir–C | 2.54 | 2.95 | 4.91 | | |
| $Ir_2$-ONC | Ir–N | 3.64 | 1.97 | 1.46 | 10.07 | 0.019 |
| | Ir–O | 1.46 | 2.09 | 3.13 | | |
| | Ir–C | 1.98 | 2.93 | 16.76 | | |
| | Ir–Ir | 0.82 | 3.09 | 0.74 | | |

**CN:** coordination number; **R:** bond distance; **$\sigma^2$:** Debye-Waller factor; **$\Delta E_0$:** the inner potential correction. **R factor:** goodness of fit.

**Table S3**. Comparison of the CER activity of $Ir_2$-ONC to that of other atomically dispersed CER catalysts reported recently in the literature.

| Catalysts | Electrolyte | TOF | Faradaic efficiency | Reference |
|---|---|---|---|---|
| **$Ir_2$-ONC** | **0.1 M $HClO_4$ + 4.0 M NaCl** | **13.51 $s^{-1}$ (E = 1.5 V vs NHE)** | **96.8%** | **This work** |
| $Ir_1$-NC | 0.1 M $HClO_4$ + 4.0 M NaCl | 7.11 $s^{-1}$ (E = 1.5 V vs NHE) | / | This work |
| $Ir_{SL}/CeO_2$ | 5 M NaCl at pH = 2 | ~28 $s^{-1}$ (E = 1.5 V vs NHE) | 99.2% | *ACS Catal.* **2024**, 14, 1962. |
| $Pt_1$/p-NC@CNTs | 0.1 M $HClO_4$ + 1.0 M NaCl | 54.5 $s^{-1}$ (η = 50 mV) | ~100% | *Adv. Funct. Mater.* **2023**, 33, 2307643 |
| $Pt_1$(3)/CNT | 0.1 M $HClO_4$ + 1.0 M NaCl | / | ~100 % | *Nat. Commun.* **2023**, 14, 3233. |
| Ru-$O_4$ SAM | 1 M NaCl at pH = 1 | 17.8 $s^{-1}$ (η = 50 mV) | 99 % | *Nat. Commun.* **2023**, 14, 2475. |
| $Pt_1/C_2N_2$ | 1 M NaCl at pH = 0.9 | 2.08 $s^{-1}$ (η = 70 mV) | 99.8% | *Small* **2023**, 19, 2300240 |
| $Ru_1$-$TiO_x$/Ti | 4 M NaCl at pH = 2 | 0.48 $s^{-1}$ (η = 50 mV) | 94.8% | *Angew. Chem. Int. Ed.* **2022**, 61, e202208215. |
| $Ir_n$-TiC | 4 M NaCl at pH = 2 | 82 $s^{-1}$ (η = 70 mV) | ~98 % | *Angew. Chem. Int. Ed.* **2022**, 61, e202200366. |
| $Pt_1$/CNT | 0.1 M $HClO_4$ + 0.1 M NaCl | / | / | *ACS Catal.* **2021**, 11, 12232. |
| $Pt_1$/CNT | 0.1 M $HClO_4$ + 1.0 M NaCl | 12 $s^{-1}$ (η = 73 mV) | 96.6% | *Nat. Commun.* **2020**, 11, 412. |

## References


1. Z. Yu, C. Si, A. P. LaGrow, Z. Tai, W. A. Caliebe, A. Tayal, M. J. Sampaio, J. P. S. Sousa, I. Amorim, A. Araujo, L. Meng, J. L. Faria, J. Xu, B. Li and L. Liu, *ACS Catal.*, 2022, **12**, 9397-9409.
2. G. Kresse and J. Furthmüller, *Phys. Rev. B*, 1996, **54**, 11169-11186.
3. G. Kresse and D. Joubert, *Phys. Rev. B*, 1999, **59**, 1758-1775.
4. J. P. Perdew, K. Burke and M. Ernzerhof, *Phys. Rev. Lett.*, 1997, **78**, 1396-1396.
5. S. Grimme, J. Antony, S. Ehrlich and H. Krieg, *J. Chem. Phys.*, 2010, **132**, 154104.
6. S. Nosé, *J. Chem. Phys.*, 1984, **81**, 511-519.
7. P. Fleurat-Lessard and T. Ziegler, *J. Chem. Phys.*, 2005, **123**.
8. C. C. L. McCrory, S. Jung, J. C. Peters and T. F. Jaramillo, *J. Am. Chem. Soc.*, 2013, **135**, 16977-16987.
9. Z. Yu, Y. Li, A. Torres-Pinto, A. P. LaGrow, V. M. Diaconescu, L. Simonelli, M. J. Sampaio, O. Bondarchuk, I. Amorim, A. Araujo, A. M. T. Silva, C. G. Silva, J. L. Faria and L. Liu, *Appl. Catal. B Environ.*, 2022, **310**, 121318.
10. Z. Yu, C. Si, F. J. Escobar-Bedia, A. P. LaGrow, J. Xu, M. J. Sabater, I. Amorim, A. Araujo, J. P. S. Sousa, L. Meng, J. L. Faria, P. Concepcion, B. Li and L. Liu, *Inorg. Chem. Front.*, 2022, **9**, 4142-4150.